

Curriculum Learning for *ab initio* Deep Learned Refractive Optics

XINGE YANG¹, QIANG FU¹, AND WOLFGANG HEIDRICH^{1,*}

¹King Abdullah University of Science and Technology, Saudi Arabia, 23955-6900

*Corresponding author: wolfgang.heidrich@kaust.edu.sa

Compiled February 3, 2023

Deep lens optimization has recently emerged as a new paradigm for designing computational imaging systems, however it has been limited to either simple optical systems consisting of a single DOE or met-alens, or the fine-tuning of a compound lenses from good initial designs. Here we present a deep lens design method based on curriculum learning, which is able to learn optical designs of compound lenses *ab initio* from randomly initialized surfaces, therefore overcoming the need for a good initial design. We demonstrate this approach with the fully-automatic design of an extended depth-of-field computational camera in a cellphone-style form factor, highly aspherical surfaces, and a short back focal length.

© 2023 Optica Publishing Group

<http://dx.doi.org/10.1364/ao.XX.XXXXXX>

1. INTRODUCTION

Deep Lens design has recently emerged as a promising new paradigm for jointly optimizing optical designs and downstream image reconstruction methods [1–6]. The Deep Lens framework is powered by differentiable optical simulators and optimization based on back propagation (or reverse mode auto-differentiation) in combination with error metrics that directly measure final reconstructed image quality rather than classical and manually tuned figures of merit. As a result, the reconstruction method (typically in the form of a deep neural network) can be learned at the same time as the optical design parameters through the use of optimization algorithms known from machine learning.

This paradigm has been applied successfully to the design of single-element optical systems composed of a single diffractive optical element (DOE) or metasurface [1, 6–11]. It has also been applied to the design of hybrid systems composed of an idealized thin lens combined with a DOE as an encoding element [3, 12–17]. In this setting, the thin lens is used as an approximate representation of a pre-existing compound lens, while the DOE is designed encode additional information for specific imaging tasks such as high dynamic range imaging [3], hyperspectral imaging [7–9], sensor super-resolution [1, 13], extended depth of field [4], or cloaking of occluders [16].

Most recently, there has been an effort to expand the deep lens design paradigm to compound optical systems composed of multiple refractive optical element [4, 5, 18–20]. The core methodology behind these efforts is optical simulation based on differentiable ray-tracing, in which the evolution of image

quality can be tracked as a function of design parameters such as lens curvatures or placements of lens elements. Unfortunately, this design space is highly non-convex, causing the optimization to get stuck in local minima, a problem that is familiar from classical optical design software [21–24]. As a result, these methods can only fine-tune good initial designs, or else require constant manual supervision, which is not suitable for joint design of optics and downstream algorithms.

In this work we eliminate the need for a good initial design and continuous manipulation in the optical lens design process by introducing an automatic method based on curriculum learning. This learning approach allows us to obtain classical optical designs fully automatically from randomly initialized lens geometries, and therefore enables the full power of Deep Lens design of compound refractive optics in combination with downstream image reconstruction. The curriculum learning approach overcomes local minima in the optimization by initially solving easier imaging tasks including a smaller aperture and field of view, and then progressively introducing more difficult design objectives. It also uses new strategies for controlling distortion and lens shapes, and effectively focusing the optimization on image regions with high error.

To illustrate the power of this new framework, we use it for designing an extended depth of field (EDoF) computational camera with cellphone-like form factor, highly aspherical lenses, and a short back focal length, where one of the lens elements has a cubic phase term added, similar to wavefront coding [25–29]. This results in an almost depth invariant PSF from which an all-in-focus image can be recovered by the reconstruction network.

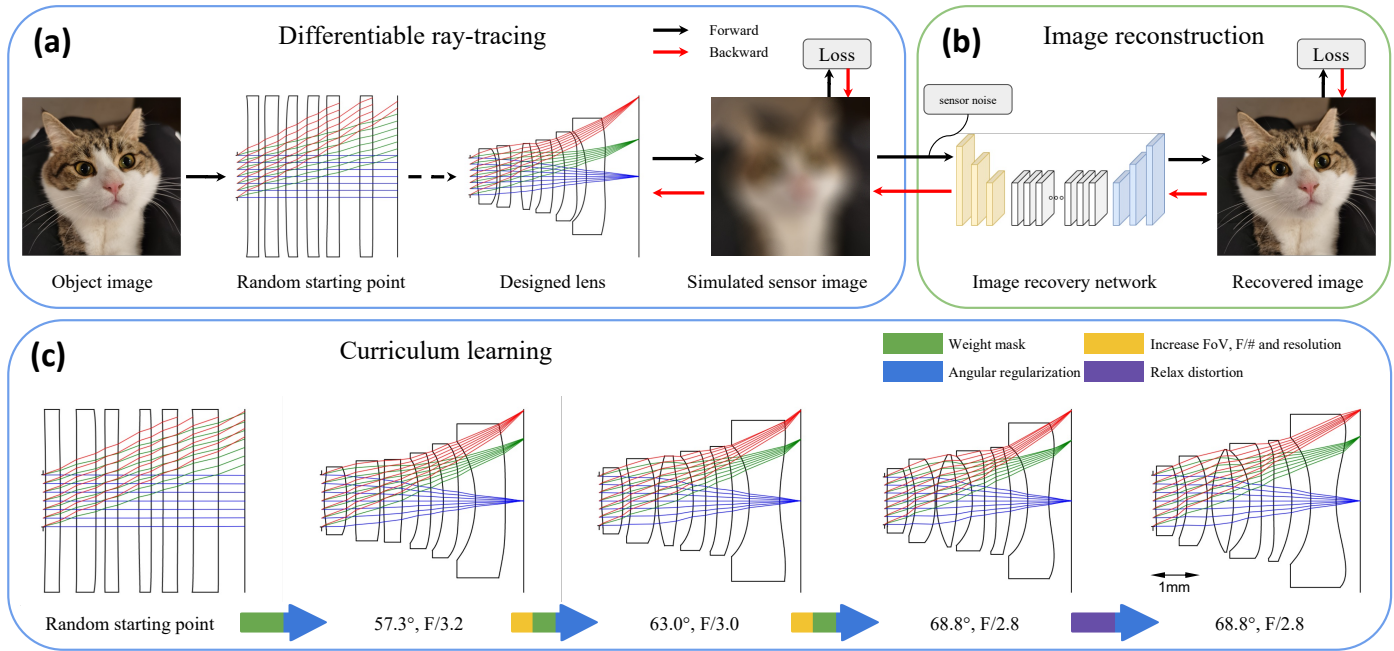


Fig. 1. Overview of the DeepLens design pipeline and curriculum learning strategy. The pipeline is composed of two modules: a differentiable ray tracing engine (a) to simulate camera sensor images, and an image recovery network (b). (a) Differentiable ray tracing learns an optical lens by directly optimizing the final image quality. In the forward pass, the sensor image is simulated by ray tracing rendering. In the backward pass, image errors are back-propagated to learn lens parameters. (b) The simulated sensor image can then be fed into the downstream image recovery network for better quality or different applications. By end-to-end learning the network and the optical lens, we can find the best match between the two modules. (c) A curriculum learning approach along with distortion and shape control strategies are proposed for fully automated lens design. Starting with a random structure, a complex optical lens can be designed without any human intervention.

To our knowledge this is the first design of an EDoF camera in this mobile device form factor, which is complicated by the strong spatial variation of aberrations across the image plane. In the supplemental material we also show several examples of classical optical designs without downstream image processing.

We believe that our proposed method bridges the gap between optical design and image processing and will lead to a general framework for any end-to-end Deep Lens design application. The code is released at <https://github.com/vccimaging/DeepLens>.

2. METHODS

A. Differentiable Ray Tracing

The deep lens optimization uses differentiable ray-tracing [4, 5, 20] as an optical simulator. Briefly, the core concept of differentiable ray-tracing is to keep track of derivative information while performing the calculations of a classical ray-tracing rendering. This allows us directly back-propagate errors in the final image quality to update optical design parameters such as lens curvatures or positions of optical elements (see Fig. 1(a)). In this way, the final image quality replaces the heuristic, hand-crafted merit functions used in conventional lens design. Crucially, the final image quality may also be assessed after a computational image reconstruction or post-processing step, allowing for the joint end-to-end optimization of the optical design and the reconstruction algorithm (Fig. 1(b)).

In particular, our work builds on top of the *dO* engine [5], which provides a memory-efficient differentiable ray-tracing framework that enables complex design tasks on desktop computers. Please see [5] and Supplement 1 for more details on the

basic differentiable ray-tracing operations.

In this work we make use of several new strategies that support fully-automated learning of designs. This includes ways to control and compensate for lens distortion as well as degenerate lens geometries, both of which are crucial during the initial stages of an optimization, when the design is still far from a feasible solution. An adjoint rendering method is also proposed to solve the memory problem in differentiable ray-tracing.

Distortion Relaxation

The straightforward way to form a loss function based on image quality is a direct pixel-wise comparison of the object plane and the image plane. This forces a reduction of geometric distortion in the optical system, while in some cases we want to relax the distortion in order to better control other optical aberrations. Then we can either correct the geometric distortion manually or design a reconstruction network to compensate for it.

To achieve this we estimate the distortion of the current design by tracing the chief rays, and then align the object and the image with image warping. An example is shown in Fig. 2(a), assuming that the lens has a barrel distortion, we pre-distort the object with the inversed pincushion distortion. This step can be done by sampling the ground truth with the original barrel distortion map. During differentiable ray-tracing, two distortions will cancel out, and the sensor image will be distortion-free. We compare sensor image with the original ground truth to compute the loss function. In this way, the distortion is excluded from the loss function, and only local aberrations are optimized.

To control the amount of permissible distortion, we optionally penalizing the magnitude of the alignment error in addition to the image quality based loss:

$$\mathcal{L} = \alpha \|\tilde{I}(I; \theta) - I\|_2^2 + (1 - \alpha) \|\tilde{I}(\mathcal{F}(I); \theta) - I\|_2^2 \quad (1)$$

where θ denotes the lens parameters, I is the ground truth image, \tilde{I} is the rendered sensor image, and $\mathcal{F}(I)$ is the warped object image. Weight coefficients α_1 and α_2 are used to balance two terms, controlling the amount of distortion. For example, $\alpha = 1$ optimizes a distortion-free lens, just like previous works.

Controlling Abnormal Shapes

To avoid abnormal lens geometries such as self-intersection during the training process, especially for the optimization of aspherical lenses, we propose an angular regularization term by penalizing the rays incident on the lens at oblique angles. It is important to note that abnormal geometries should be avoided, not only for the numerical stability of the optimization process, but also to improve the manufacturing tolerances of the final design. As shown in Fig. 2(b), the angular regularization term maximizes the dot products of the incident rays and the surface normal, as follows:

$$\mathcal{L}_{reg} = \sum_k^{spp} \prod_m^M \mathbf{d}_{km} \cdot \mathbf{n}_{km}, \quad (2)$$

where spp is the number of rays sampled from each pixel, and M is the number of lens surfaces. \mathbf{d} and \mathbf{n} are normalized ray direction and surface normal vector, respectively. For implementation, we track an additional term in the ray tracing process to record the incident angularity information. Experimental results show that this angular regularization helps to design smooth optical paths and avoid self-intersecting lens surfaces during the optimization process.

For more details and implementations of above discussed methods, see [Supplement 1](#).

Adjoint Rendering for Memory Saving

End-to-end training of differentiable ray-tracing consumes a large amount of memory. Existing approaches either compute adjoint derivatives [30, 31] in the forward pass, simplify intermediate computations [5], or use small sensor resolutions and spp [4]. We overcome this problem by recalculating the ray-tracing rendering during backpropagation, as in [32]. First, we perform a ray-tracing rendering to simulate the sensor image without tracking gradient information. Then, we feed the image into the reconstruction network and back-propagate the gradients to update the network to obtain an error image. Finally, we re-perform differentiable ray-tracing and back-propagate the error image to obtain the lens gradient. In experiments, this adjoint rendering approach coupled with a patch segmentation strategy reduces the memory consumption to a constant level.

B. Curriculum Learning for Automatic Lens Design

Designing a complex imaging lens is a highly non-convex problem, as the search space contains a large amount of local minima, saddle points and flat regions [22–24], which may cause the design process to get stuck in configurations that are locally optimal but have poor performance globally. During the optimization, the lens is often led to destructive structures, such as self-intersection and aggressive aspherical shapes. Conventional lens design methods are incapable of addressing these corrupted structures and therefore require the manual intervention of an experienced optical engineer in the optimization process. Control of distortions and degenerate geometries helps reduce the

issues especially early in the optimization process, but they do not prevent local minima later on.

To overcome local minima and enable fully automatic design, we adopt a curriculum learning approach, whereby the final design goal is broken down into steps that progress from an easy design task to progressively harder tasks until the ultimate goal is achieved. Specifically, our curriculum for lens design is based on two well-known observations: 1) geometric optics aberrations are minimized for small apertures, and 2) paraxial regions are less aberrated than large angles. Consequently the lens design curriculum starts by optimizing the lens for a small aperture and field of view and gradually increasing both to the final design specifications.

As shown in Fig 1(c), we can directly optimize an imaging lens from several planes. The first lens design (57.3°, F/3.2) does not have an aggressive shape because the target is easy. Then we gradually increase the FoV and F-number, but only slightly at each step so that the increase in difficulty stays within a reasonable range (63.0°, F/3.0). As the optimization proceeds, the lens shape becomes more and more complex, as shown in Fig. 1(c). Finally we increase FoV and F-number to the design target (68.8°, F/2.8), and after fine-tuning we can obtain an imaging lens with optical performance close to the diffraction limit. The curriculum strategy with increasing FoV and F-number can be understood as follows: larger aperture sizes introduce more off-axis rays that are difficult to converge, while large FoV rays are more sensitive to surface shape according to Snell's law. Therefore, directly designing large FoV and F-number is more likely to fail. In contrast, starting with smaller apertures and FoV making the optimization easier.

Another part of the lens design curriculum is a mechanism by which the optimization can focus on improving a certain region of the image plane. Especially when designing highly aspherical lenses, it is possible to arrive at local minima where most of the image is sharp, but some small regions still suffer from aberrations. In this situation the overall image gradient may not be sufficient to get out of this local minimum. Instead, we introduce a dynamic weight mask that can automatically focus on improving problem regions (see Fig. 2(c)). To form the weight mask, we first calculate the per-pixel spot RMS error and then apply an activation function to it. The weight mask M is computed at the beginning of each training epoch. Then, the problem regions will have a higher weight in this training epoch. With the weight mask, the complete loss function can be written as

$$\mathcal{L} = \|M(\tilde{I} - I)\|_2^2 - \omega \mathcal{L}_{reg} \quad (3)$$

where ω is the weight term for the angular regularization.

The proposed curriculum learning approach enables us to optimize a complex lens from a random initialization starting point without any intervention. An example is shown in [video](#). Please check [Supplement 1](#) for detailed implementations and results.

C. End-to-end Learning for Extended-Depth-of-Field Imaging

Differentiable ray-tracing simulates and optimizes the sensor image, which enables us to feed the image into the downstream network and jointly optimize the network and the lens. This co-design idea has been superior to conventional single-part optimization in many applications [3–5, 12, 33–35]. Specifically, we focus on extended-depth-of-field (EDoF) imaging, which aims to obtain all-in-focus images over a wide range of depths. Clas-

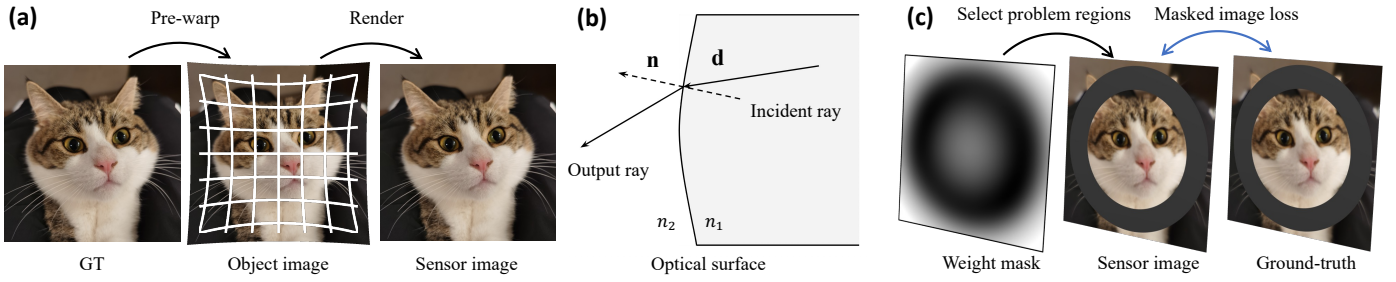


Fig. 2. Strategies used in the curriculum learning approach. (a) To allow for geometric distortion in the final designed lens, we can relax the distortion during the training. For example, if a lens has barrel distortion, we pre-warp the ground truth image with a pincushion distortion and use the result as the object image. The sensor image is distortion-free compared to the ground truth image. (b) We penalize rays with large incident angle $\langle d, n \rangle$, which may lead to anomalous surface shapes. (c) A weight mask is used to dynamically improve a region of the image plane to bring the optimization away from local minima.

sical imaging lenses suffer from a shallow depth-of-field when using a large aperture, but computational cameras can exceed this constraint. The odd-polynomial surfaces (e.g., cubic phase) has the property of producing depth-independent PSFs [36–39] and are therefore used to form an EDoF lens. The height profile of an odd-polynomial surface can be written as:

$$z(x, y) = \sum_{i=1}^n (a_i x^{2i+1} + b_i y^{2i+1}), \quad (4)$$

where coordinates $\{a_1, \dots, a_n\}$ and $\{b_1, \dots, b_n\}$ are optimizable coefficients, and n is the polynomial degree. The degree n is user-defined and can be increased to allow for finer control of the surface height profile, in the experiments we used $n = 2$.

A common way to use the odd-polynomial surface is to insert a plate at the aperture position, which is usually the first surface of a smartphone lens. In addition, we investigate an aspheric-odd-polynomial hybrid surface to replace the first surface of the original imaging lens. This hybrid surface is formed by combining an aspheric surface with an odd-polynomial surface:

$$z(r) = \underbrace{\frac{r^2}{R(1 + \sqrt{1 - (1 + \kappa)r^2/R^2})}}_{\text{aspherical}} + \alpha_2 r^2 + \alpha_4 r^4 + \dots + \underbrace{\sum_{i=1}^n (a_i x^{2i+1} + b_i y^{2i+1})}_{\text{odd-polynomial}}. \quad (5)$$

where the first part is an aspherical surface. $r = \sqrt{x^2 + y^2}$ is the distance from the axis, R is the radius of curvature, κ is the conic, and α_i are the the polynomial coefficients of the aspherical surface.

As a trade-off, the odd-polynomial surface produces much larger PSFs, which blurs the sensor image. Therefore, an image reconstruction network is necessary after capturing sensor images. We then jointly optimize the odd-polynomial polynomial coefficients and the network to find the best match between the two components. We used NAFNet [40] as the image reconstruction network without modifying the architecture. NAFNet is a UNet-shaped network with optimized inter- and intra-blocks, making it computationally efficient and easy to train. In addition, NAFNet shows SOTA performance on several image deblurring tasks when we conducted experiments. Considering the balance between performance and computational efficiency, we believe it is well suited for our end-to-end EDoF training.

Following the idea of the curriculum learning, we first design a good imaging lens and then optimize the odd-polynomial coefficients for EDoF imaging. After obtaining the imaging lens, we no longer use the weight mask and angular regularization. A white Gaussian noise of $\sigma = 0.001$ is added to simulate the sensor noise. Taking advantage of modern advances in image recovery techniques, we design a loss function with pixel-level loss and perceptual loss to obtain the best output quality. To obtain similar images over the extended depth range, we used a regularization term to minimize the differences in the simulated images. The total functional loss is:

$$\mathcal{L} = \sum_d [\mathcal{L}_{\text{pixel}}(\tilde{I}_d, I) + \alpha_1 \mathcal{L}_{\text{percep}}(\tilde{I}_d, I)] + \alpha_2 \sum_{d \neq d'} \mathcal{L}_{\text{sim}}(\tilde{I}_d, \tilde{I}_{d'}), \quad (6)$$

where I is the ground truth image, \tilde{I} is the simulated sensor image, and \tilde{I} is the recovered image. d is the depth of object image, in the experiment we discrete the continuous depth range into a list of training depths. In our experiments, we use PSNR loss as pixel loss, VGG loss [41] as perceptual loss, and l_2 loss as similarity loss. To save memory and time, in each iteration we only select two different depths for training. α_1 and α_2 are weight factors to balance different losses for the best results. For more training details about the implementation and experiment settings, please refer to [Supplement 1](#).

3. RESULTS

In this section, we evaluate the proposed curriculum learning approach by designing an EDoF lens from scratch. The EDoF lens is designed to have a large aperture size with a wide depth of field, allowing us to image clearly from 20cm to 10m even in low light.

Following the idea of curriculum learning, we first design an classical imaging lens. The starting point is formed with several randomly placed and initialized surfaces, and the lens materials are pre-determined. We design the lens with a focal length of 7.66mm, FoV 57.3°, F/3.2, and the aperture diameter is 2.19mm, the image height is 7.6mm. As shown in Fig. 1(c), the designed lens has a similar shape to commonly used smartphone lenses, while no prior knowledge or human intervention is provided during the whole designing process. For detailed lens data and more lens design examples, please see [Supplement 1](#).

A large aperture causes a significant depth-of-field (DoF) effect when the lens is focused to a short distance. In our experiments, we focus the lens to a distance of 45cm and evaluate

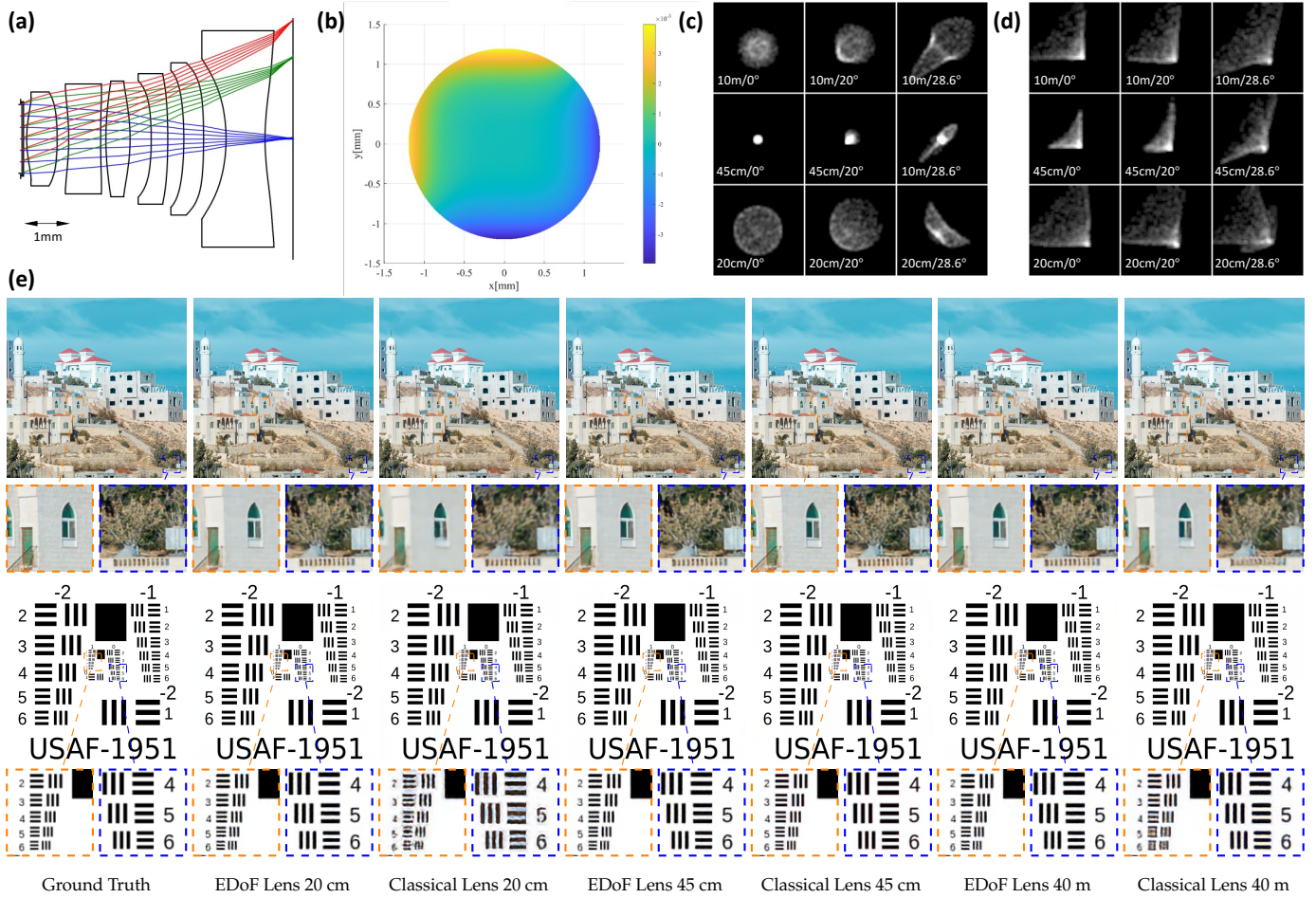


Fig. 3. Qualitative comparison between the end-to-end learned EDoF lens and the classical lens with network recovery. (a) The designed imaging lens has a similar structure with commonly used smartphone lenses, but no human knowledge or intervention is used during the optimization process. An odd-polynomial plate is added to front of the imaging lens for EDoF imaging. (b) The end-to-end learned height profile of the odd-polynomial surface. (c) The PSF of the original imaging lens. The lens is focused to 45 cm, thus PSF at 20 cm and 10 m is much larger than that at 45 cm, causing a DoF effect. (d) The PSF of the end-to-end learned EDoF lens. The PSF is larger than that of the classical lens, but it is similar at different depths and view angles. The lens aberration degrades this similarity, but the recovery network can compensate for it. (e) Recovered results of the final output of the EDoF lens and the classical lens. Upper: a landscape image. Lower: USAF-1951 resolution chart. The EDoF lens can produce clear images at different depths, while the recovery results of the classical lens are still focus-dependent and contain artifacts.

its imaging performance between 20cm and 10m. We select 15 depths and calculate the average PSNR/SSIM scores of 100 1024×1024 test images at each depth to quantify the imaging quality. As shown in Fig. 4, the green curve indicates a significant DoF effect, meaning the classical imaging lens can not image clearly outside the focus range. See also Fig. 3(c), the PSF at 20cm and 10m is much larger than the PSF at 45cm. And at large view angles, the lens suffers from off-axis aberrations.

We then insert an odd-polynomial plate (Fig.3(a)) in front of the lens for EDoF imaging. In the following part, the new lens is referred to as "EDoF lens" and the original imaging lens is "classical lens". The odd-polynomial surface has a radius of 2.40mm and a thickness of 0.05mm. The glass material is H-BK7 ($n_d = 1.5168$, $V_d = 64.17$) and the front surface of the plate is the odd-polynomial surface. After image simulation, a deep network is utilized to recover the sensor image. We jointly optimize the EDoF lens and the network to produce clear images from 20cm to 10m. To avoid overfitting and reduce complexity, we discrete the continuous depth range into 7 training depths (20 cm, 30 cm, 45 cm, 70 cm, 1 m, 2 m, 10 m) that are uniformly

chosen from the green curve in Fig. 4. During the end-to-end training, we place object images at different depths and simulate sensor images. Then we recover the sensor images by the network, and perform back-propagation to optimize the lens and the network together. Three wavelengths (486 nm, 587 nm, and 656 nm) are used to render different image channels, allowing the network to learn to minimize the chromatic aberration caused by the odd-polynomial plate. For more information on the training process, please see Supplement 1.

Fig. 3(a) shows the final design of the EDoF lens, and Fig. 3(b) shows the height profile of the odd-polynomial surface. In Fig. 3(d), the EDoF lens exhibits triangle-shaped PSF that is nearly depth independent. Although the PSF varies slightly at different depths and view angles, the network is robust enough to compensate for these differences. The imaging quality of the EDoF lens is inferior to that of the classical lens (shown by the red and green curve in Fig. 4), but remains unchanged over a board depth range. After image recovery by the deep network, the output quality of the EDoF lens significantly improves and displays little DoF effect (shown by the blue curve in Fig. 4).

Table 1. Quantitative comparison on different EDoF methods in terms of PSNR(dB)/SSIM.

Method	Classical Lens		EDoF Lens (Odd-polynomial plate)		EDoF Lens (Hybrid surface)	
	imaging	recovery	imaging	recovery	imaging	recovery
20 cm	24.71/0.670	27.80/0.787	22.90/0.611	30.27/0.860	24.78/0.706	29.36/0.844
45 cm	27.82/0.842	31.27/0.890	22.99/0.620	30.81/0.873	25.16/0.722	31.07/0.885
10 m	25.54/0.700	28.45/0.808	23.46/0.632	30.17/0.854	24.78/0.687	30.17/0.862

On the test dataset, the end-to-end learned EDoF lens produces PSNR scores greater than 30dB and SSIM scores greater than 0.85 at all depths within the extended depth range (Fig. 4). At 20 cm, 45 cm, and 10 m, the output results show significant improvement of approximately 5.5 dB, 3 dB, and 4.5 dB beyond the classical lens imaging results (Tab. 1). Fig. 3(e) shows zoomed patches of the recovered images, the recovered images of the end-to-end learned EDoF lens closely resemble the ground-truth object images at different depths (20 cm, 45 cm, 10 m) while preserving details well.

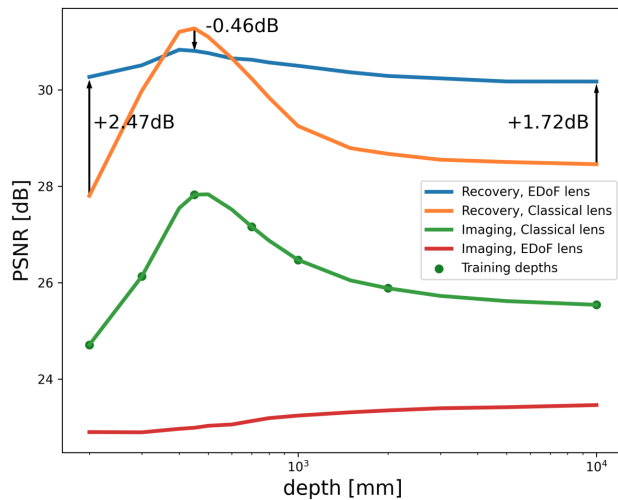


Fig. 4. PSNR curve of EDoF imaging results. Green: the designed large aperture lens has DoF effect and can not image clearly outside the focal range. Orange: although a reconstruction network can improve image quality, it can not eliminate the DoF effect. Blue: our end-to-end learned EDoF lens and the reconstruction network can output clear images over a wide range of depths, with a significant improvement over both the imaging lens and pure network reconstruction. Red: sensor captured images of the EDoF lens are worse than the imaging lens, but almost depth-independent.

For comparison, we train a network to recover the sensor images of the classical lens, simulating image post-processing in modern cameras. This is a blind deblurring task as the depth of object images is unknown, and the DoF effect causes out-of-focus object images to appear blurry. To achieve the best recovery results, we focused on optimize the output quality without minimizing the similarity between different depths. For a fair comparison, we use the same network architecture and training process as in the end-to-end training experiment. Shown in Fig. 4, the network improves the image quality of the classical lens but is unable to eliminate the DoF effect (orange curve). The recovery network is focus-dependent and out-of-focused images can not be recovered well. From Tab. 1, the EDoF lens loses only 0.46 dB at the in-focus depth (45 cm), but gains 2.47 dB and

1.72 dB at 20 cm and 10 m, respectively. This trade-off is acceptable in most cases, especially since the end-to-end learned EDoF can already image clearly. The recovered images are shown in Fig. 3(e). The images at 45 cm are the closest to the ground-truth, since the lens is focused at this distance and the simulated images are clear. The recovered images at 20 cm and 10 m are still very blurry and contain significant recovery artifacts. In contrast, the EDoF lens results have no artifacts and are clearer than the classical lens.

We also examine the hybrid aspherical-odd-polynomial surface described in Eq. 5. In the experiments, we substitute the back surface of the first element of the original imaging lens with this hybrid surface. And then we jointly optimize the lens and the recovery network for EDoF imaging. The quantitative results are reported in Tab. 1, The imaging performance of the hybrid-surface EDoF lens is better than the previous EDoF lens. Additionally, this hybrid-surface EDoF lens has the advantage of a more compact structure. The final recovery results are similar with the previous EDoF lens. Detailed lens data, as well as qualitative and quantitative results of this hybrid-surface EDoF lens, can be found in Supplement 1. We believe this hybrid-surface EDoF lens is more practical due to its compact structure.

4. CONCLUSION

We present a fully automated approach to refractive lens design. With the curriculum learning strategy, we can design any refractive lens system from scratch without any prior knowledge or human intervention. We also propose multiple approaches to control lens distortion, avoid abnormal surface shapes, and reduce the memory consumption of differentiable ray tracing. To the best of our knowledge, this is the first work to apply differentiable ray tracing to pure optical design and achieve performance as good as that of conventional lens design methods.

In addition, we end-to-end designed a computational lens with an image recovery network for EDoF imaging. Experimental results show that the designed EDoF lens can image clearly over a wide depth range and surpasses the classical lenses with image recovery. Compared with existing work [1, 4, 39], our designed EDoF lens has a larger extended depth range (20 cm to 10 m) and a larger field of view (57.3°), enabling the technique to be used in a wider range of applications. The designed EDoF lens is based on a smartphone-shaped lens, which also provides the possibility of designing EDoF lenses for next-generation smartphone cameras.

However, there are still some shortcomings in our work. First, we did not fabricate the designed lens and test its optical performance. Instead, we only evaluated it in the commercial software Zemax. Second, we did not take into account the diffraction of the lens, reducing the accuracy of the simulation. We also did not include diffractive optical elements in our lens system. However, we have started to study this topic and hope to close

this gap.

Funding. King Abdullah University of Science and Technology (Individual Baseline Funding).

Disclosures. The authors declare no conflicts of interest.

Data availability. Code should be publicly available at: <https://github.com/vccimaging/DeepLens>.

Supplemental document. See Supplemental Document 1 for supporting content.

REFERENCES

1. V. Sitzmann, S. Diamond, Y. Peng, X. Dun, S. Boyd, W. Heidrich, F. Heide, and G. Wetzstein, "End-to-end optimization of optics and image processing for achromatic extended depth of field and super-resolution imaging," *ACM Trans. Graph.* **37** (2018).
2. G. Wetzstein, A. Ozcan, S. Gigan, S. Fan, D. Englund, M. Soljačić, C. Denz, D. A. Miller, and D. Psaltis, "Inference in artificial intelligence with deep optics and photonics," *Nature* **588**, 39–47 (2020).
3. Q. Sun, E. Tseng, Q. Fu, W. Heidrich, and F. Heide, "Learning rank-1 diffractive optics for single-shot high dynamic range imaging," in *Proceedings of the IEEE/CVF conference on computer vision and pattern recognition*, (2020), pp. 1386–1396.
4. Q. Sun, C. Wang, F. Qiang, D. Xiong, and H. Wolfgang, "End-to-end complex lens design with differentiable ray tracing," *ACM Trans. Graph.* **40**, 1–13 (2021).
5. C. Wang, N. Chen, and W. Heidrich, "dO: A differentiable engine for Deep Lens design of computational imaging systems," *IEEE Trans. Comput. Imaging* (2022).
6. E. Tseng, S. Colburn, J. Whitehead, L. Huang, S.-H. Baek, A. Majumdar, and F. Heide, "Neural nano-optics for high-quality thin lens imaging," *Nat. Commun.* **12**, 1–7 (2021).
7. D. S. Jeon, S.-H. Baek, S. Yi, Q. Fu, X. Dun, W. Heidrich, and M. H. Kim, "Compact snapshot hyperspectral imaging with diffracted rotation," *ACM Trans. Graph.* (2019).
8. X. Dun, H. Ikoma, G. Wetzstein, Z. Wang, X. Cheng, and Y. Peng, "Learned rotationally symmetric diffractive achromat for full-spectrum computational imaging," *Optica* **7**, 913–922 (2020).
9. S.-H. Baek, H. Ikoma, D. S. Jeon, Y. Li, W. Heidrich, G. Wetzstein, and M. H. Kim, "Single-shot hyperspectral-depth imaging with learned diffractive optics," in *Proceedings of the IEEE/CVF International Conference on Computer Vision*, (2021), pp. 2651–2660.
10. I. Chugunov, S.-H. Baek, Q. Fu, W. Heidrich, and F. Heide, "Mask-ToF: Learning microlens masks for flying pixel correction in time-of-flight imaging," in *Proceedings of the IEEE/CVF Conference on Computer Vision and Pattern Recognition*, (2021), pp. 9116–9126.
11. L. Li, L. Wang, W. Song, L. Zhang, Z. Xiong, and H. Huang, "Quantization-aware deep optics for diffractive snapshot hyperspectral imaging," in *Proceedings of the IEEE/CVF Conference on Computer Vision and Pattern Recognition*, (2022), pp. 19780–19789.
12. J. Chang and G. Wetzstein, "Deep optics for monocular depth estimation and 3d object detection," in *Proceedings of the IEEE/CVF International Conference on Computer Vision*, (2019), pp. 10193–10202.
13. Q. Sun, J. Zhang, X. Dun, B. Ghanem, Y. Peng, and W. Heidrich, "End-to-end learned, optically coded super-resolution spad camera," *ACM Trans. on Graph. (TOG)* **39**, 1–14 (2020).
14. C. A. Metzler, H. Ikoma, Y. Peng, and G. Wetzstein, "Deep optics for single-shot high-dynamic-range imaging," in *Proceedings of the IEEE/CVF Conference on Computer Vision and Pattern Recognition*, (2020), pp. 1375–1385.
15. H. Ikoma, C. M. Nguyen, C. A. Metzler, Y. Peng, and G. Wetzstein, "Depth from defocus with learned optics for imaging and occlusion-aware depth estimation," in *2021 IEEE International Conference on Computational Photography (ICCP)*, (IEEE, 2021), pp. 1–12.
16. Z. Shi, Y. Bahat, S.-H. Baek, Q. Fu, H. Amata, X. Li, P. Chakravarthula, W. Heidrich, and F. Heide, "Seeing through obstructions with diffractive cloaking," *ACM Trans. Graph.* **41**, 1–15 (2022).
17. S. Pinilla, S. R. M. Rostami, I. Shevkunov, V. Katkovnik, and K. Egiazarian, "Hybrid diffractive optics design via hardware-in-the-loop methodology for achromatic extended-depth-of-field imaging," *Opt. Express* **30**, 32633–32649 (2022).
18. G. Côté, J.-F. Lalonde, and S. Thibault, "Deep learning-enabled framework for automatic lens design starting point generation," *Opt. Express* **29**, 3841–3854 (2021).
19. S. Chen, T. Lin, H. Feng, Z. Xu, Q. Li, and Y. Chen, "Computational optics for mobile terminals in mass production," *IEEE Trans. Pattern Anal. Mach. Intell.* (2022).
20. X. Yang, Q. Fu, and W. Heidrich, "Automatic lens design based on differentiable ray-tracing," in *Imaging and Applied Optics Congress 2022 (3D, AOA, COSI, ISA, pcAOP)*, (Optica Publishing Group, 2022), p. CTh4C.2.
21. W. J. Smith, *Modern optical engineering: the design of optical systems* (McGraw-Hill Education, 2008).
22. Y. Ma *et al.*, "Design of a 16.5 megapixel camera lens for a mobile phone," *Open Access library journal* **2**, 1 (2015).
23. Y. T. Liu, "Review and design a mobile phone camera lens for 21.4 mega," Ph.D. thesis, University of Arizona (2017).
24. J. Joo and H. Alisafae, "Optimization of a mobile phone camera for as-built performance," in *Current Developments in Lens Design and Optical Engineering XXI*, vol. 11482 (SPIE, 2020), pp. 85–94.
25. C. Wang, Q. Fu, X. Dun, and W. Heidrich, "Quantitative phase and intensity microscopy using snapshot white light wavefront sensing," *Sci. Rep.* **9**, 1–12 (2019).
26. L. Dong, H. Du, M. Liu, Y. Zhao, X. Li, S. Feng, X. Liu, M. Hui, L. Kong, and Q. Hao, "Extended-depth-of-field object detection with wavefront coding imaging system," *Pattern Recognit. Lett.* **125**, 597–603 (2019).
27. C. Wang, Q. Fu, X. Dun, and W. Heidrich, "Modeling classical wavefront sensors," *Opt. Express* **28**, 5273–5287 (2020).
28. C. Wang, N. Chen, and W. Heidrich, "Towards self-calibrated lens metrology by differentiable refractive deflectometry," *Opt. Express* **29**, 30284–30295 (2021).
29. U. Akpınar, E. Sahin, M. Meem, R. Menon, and A. Gotchev, "Learning wavefront coding for extended depth of field imaging," *IEEE Trans. Image Process.* **30**, 3307–3320 (2021).
30. M. Nimier-David, S. Speierer, B. Ruiz, and W. Jakob, "Radiative back-propagation: An adjoint method for lightning-fast differentiable rendering," *ACM Trans. Graph.* **39** (2020).
31. A. Teh, M. O'Toole, and I. Gkioulekas, "Adjoint nonlinear ray tracing," *ACM Trans. Graph.* **41**, 1–13 (2022).
32. D. Vicini, S. Speierer, and W. Jakob, "Path replay backpropagation: Differentiating light paths using constant memory and linear time," *ACM Trans. Graph.* **40**, 108:1–108:14 (2021).
33. H. Haim, S. Elmalem, R. Giryas, A. M. Bronstein, and E. Marom, "Depth estimation from a single image using deep learned phase coded mask," *IEEE Trans. Comput. Imaging* **4**, 298–310 (2018).
34. Y. Peng, Q. Sun, X. Dun, G. Wetzstein, W. Heidrich, and F. Heide, "Learned large field-of-view imaging with thin-plate optics," *ACM Trans. Graph.* **38**, 219–1 (2019).
35. E. Tseng, A. Mosleh, F. Mannan, K. St-Arnaud, A. Sharma, Y. Peng, A. Braun, D. Nowrouzezahrai, J.-F. Lalonde, and F. Heide, "Differentiable compound optics and processing pipeline optimization for end-to-end camera design," *ACM Trans. Graph.* **40**, 1–19 (2021).
36. E. R. Dowski and W. T. Cathey, "Extended depth of field through wavefront coding," *Appl. Opt.* **34**, 1859–1866 (1995).
37. S. Chen, Z. Fan *et al.*, "Optimized asymmetrical tangent phase mask to obtain defocus invariant modulation transfer function in incoherent imaging systems," *Opt. letters* **39**, 2171–2174 (2014).
38. L. Yang, M. Chen, J. Wang, M. Zhu, T. Yang, S. Zhu, and H. Xie, "Extended depth-of-field of a miniature optical endoscope using wavefront coding," *Appl. Sci.* **10**, 3838 (2020).
39. C.-F. Lee and C.-C. Lee, "Microscope with extension of the depth of field by employing a cubic phase plate on the surface of lens," *Results Opt.* **4**, 100107 (2021).
40. L. Chen, X. Chu, X. Zhang, and J. Sun, "Simple baselines for image restoration," *arXiv preprint arXiv:2204.04676* (2022).

41. C. Ledig, L. Theis, F. Huszár, J. Caballero, A. Cunningham, A. Acosta, A. Aitken, A. Tejani, J. Totz, Z. Wang *et al.*, "Photo-realistic single image super-resolution using a generative adversarial network," in *Proceedings of the IEEE conference on computer vision and pattern recognition*, (2017), pp. 4681–4690.